The Astrophysical Journal, 708:742–749, 2010 January 1 doi:10.1088/0004-637X/708/1/742

DETECTION OF A SUPERSTRONG 2175 Å ABSORPTION GALAXY AT $z = 0.8839$ TOWARD THE QUASAR SDSS J100713.68+285348.4

Hongyan Zhou[1,2,3,4], Jian Ge[3], Honglin Lu[1,2], Tinggui Wang[1], Weimin Yuan[5], Peng Jiang[1,3], and Hongguang Shan[5]
[1] Key Laboratory for Research in Galaxies and Cosmology, The University of Sciences and Technology of China, Chinese Academy of Sciences, Hefei, Anhui 230026, China
[2] Max-Planck-Institut für extraterrestrische Physik, Postfach 1312, 85741 Garching, Germany
[3] Department of Astronomy, University of Florida, Gainesville, FL 32611, USA
[4] Center for Astrophysics, University of Science and Technology of China, Hefei, Anhui 230026, China
[5] National Astronomical Observatories/Yunnan Observatory, Chinese Academy of Sciences, Kunming, Yunnan 650011, China
Received 2009 June 26; accepted 2009 November 12; published 2009 December 15

ABSTRACT

We report a superstrong 2175 Å absorption galaxy at a redshift of $z_G = 0.8839$ toward the background quasar SDSS J100713.68+285348.4 at $z_Q = 1.047$ identified from the Sloan Digital Sky Survey (SDSS) data. The bump is the strongest ever known, about 2.5 times the average in the Galactic interstellar extinction curves. About two dozens of narrow absorption lines are identified in this system in the SDSS and the follow-up Multiple Mirror Telescope (MMT) spectra, including Zn II, Cr II, Mn II, Si II, Fe II, Ti II, Ca II, Al III, Mg II, and Mg I. We have derived accurate measurements of the gas-phase column densities of most of these ions through their weak absorption lines. The combination of unprecedentedly strong 2175 Å absorption bump strength with the measured zinc column density suggests that carbon is likely to be the main carrier of the 2175 Å absorber assuming that the total abundance of the absorber relative to zinc is similar to the solar values and zinc is not heavily depleted onto dust grains. Under the same assumption, we found that dust depletion in this absorption galaxy is much less than that in the Milky Way, indicating possible different nucleosynthesis and/or chemical and interstellar medium evolution history.

Key words: dust, extinction – quasars: absorption lines – quasars: individual (SDSS J1007+2853)

Online-only material: color figures

1. INTRODUCTION

The 2175 Å bump is the most prominent spectral feature in the interstellar extinction curves of the Milky Way (MW). All of the observed MW extinction curves in the region of the bump can be very well reproduced by the Drude profile combined with a linear background (Fitzpatrick & Massa 1986, 1990, 2005, 2007; hereafter FM86, FM90, FM05, FM07, respectively),

$$\frac{E(x-V)}{E(B-V)} = c_1 + c_2 x + \frac{c_3 x^2}{\left(x^2 - x_0^2\right)^2 + \gamma^2 x^2}, \qquad (1)$$

where $x \equiv 1/\lambda$ is inverse wavelength. The bump strength is either expressed by the peak extinction relative to the underlying background, $H = c_3/\gamma^2$, or more appropriately by the total relative extinction underneath the bump profile $A = \pi c_3/2\gamma$. The latter is proportional to the absorption equivalent width relative to $E(B-V)$ measured in units of wavenumber (Whittet 1992). The central position of the bump is nearly a constant. It peaks at $\lambda = 2175$ Å, with a mean deviation of 9 Å. The bump width varies from 360 Å to 770 Å for the MW, with a typical value of ~480 Å (Tielens 2005). The bump strength of the MW can also vary severalfold (FM07; see also Figure 4).

Although the strong broad 2175 Å UV absorption bump and their strengths are strongly correlated with the interstellar dust grain population (Draine 2003), the nature of the absorption carrier remains enigmatic after more than 40 years of extensive study since the discovery of the 2175 Å bump (Stecher 1965). Draine (1989) was able to narrow down the candidate for the carrier to one or more of C, Mg, Si, and Fe based on the following abundance arguments. The number of absorbers per H atom can be estimated as

$$\frac{N_{2175}}{N_H} = \frac{m_e c}{\pi e^2} \frac{0.921 A}{f_{2175}} \frac{E(B-V)}{N_H} \gtrsim 10^{-5}, \qquad (2)$$

where $f_{2175} \lesssim 1$ is the oscillator strength per absorber,[6] and we have used the observed MW average bump strength of $A \approx 4.73\ \mu\mathrm{m}^{-1}$ (FM07), and a gas-to-dust ratio of $N_H/E(B-V) \approx 4.93 \times 10^{21}$ cm^{-2} (Diplas & Savage 1994). Metals more abundant than $N_X/N_H = 10^{-5}$ include O (7.4×10^{-4}), C (3.5×10^{-4}), N (1.0×10^{-4}), Ne (1.0×10^{-4}), Mg (3.8×10^{-5}), Si (3.5×10^{-5}), Fe (3.2×10^{-5}), and S (1.9×10^{-5}), where the candidate elements are lower-lineated (Savage & Sembach 1996). Because Ne is a noble gas, and both O and N are electron acceptors, these three elements can be readily excluded from the candidate list. S is also unlikely a candidate since its solar abundance is only about two times that of the threshold value and its depletion to dust grains in the diffuse interstellar medium (ISM) is negligible. Therefore, only C, Mg, Si, and Fe are left as candidate carriers. Identification of extragalactic 2175 Å absorbers with strong bump strengths and different abundance patterns can possibly provide further constraints on the nature of the 2175 Å absorber carrier.

Only a few handful individual detections of the 2175 Å bump outside the MW have been reported in literature. Precise measurements of extinction curves are almost exclusively limited in the Local Group, where it is possible to study individual stars. The 2175 Å bump is detected in Large Magellanic Cloud

[6] The oscillator strength per absorber atom of even a very strong permitted transition is typically less than $0.5\nu_e$, where ν_e is the number of electrons that can participate in the transition (e.g., Draine 1989).

(LMC; e.g., FM86) and in a few regions of Small Magellanic Cloud (SMC; Lequeux et al. 1982; Cartledge et al. 2005) with a strength of ∼50% of the average MW value. Beyond the Local Group, detections of the bump are made using quasars (see Wang et al. 2004 for an early review; Srianand et al. 2008; Noterdaeme et al. 2009) or γ-ray bursts (e.g., Ellison et al. 2006; Schady et al. 2007; Krühler et al. 2008) as background light sources, and measurements of the bump are at best given as "present" or "absent."

In this paper, we report the discovery of a superstrong 2175 Å absorption galaxy toward the quasar SDSS J100713.68+285348.4 (hereafter "SDSS J1007+2853G" when referring to the absorption galaxy and "SDSS J1007+2853" to the background quasar). The bump is the strongest known thus far. This for the first time enables a measurement of the bump beyond the Local Group at a similar accuracy as in the MW. Many narrow absorption lines (NALs) of interest are detected at a common redshift of $z_G = 0.8839 \pm 0.0002$, allowing reliable measurements of the gas-phase abundances and dust depletion in SDSS J1007+2853G. The organization of the paper is as follows. The data used will be described in Section 2. We will derive and fit the extinction curve in Section 3. We will measure metal column densities from the NAL spectrum in Section 4, and discuss straightforward implications in Section 5. Throughout this paper, we will adopt a cosmology with $H_0 = 70$ km s^{-1} Mpc^{-1}, $\Omega_M = 0.3$, and $\Omega_\Lambda = 0.7$.

2. OBSERVATION AND DATA REDUCTION

SDSS J1007+2853 was selected as a candidate 2175 Å absorber in a systematic search for such objects according to its very red Sloan Digital Sky Survey (SDSS) spectra (Section 2.1) and broadband spectral energy distribution (SED; Section 2.2), which was confirmed by our follow-up MMT spectroscopy (Section 2.3). All of the data have been corrected for the Galactic reddening of $E(B - V) = 0.023$ (Schlegel et al. 1998) before further analysis.

2.1. *Sloan Digital Sky Survey Spectra*

SDSS J1007+2853 was targeted for spectroscopic observations by the SDSS (York et al. 2000) as an optical counterpart of a radio source detected by Faint Images of the Radio Sky at Twenty-cm (FIRST; White et al. 1997). Two observations were taken at 2006 January 22 with total exposures of 2520 and 3300 s respectively. Eighty percent seeing during the observations is 1″.3, much less than the SDSS fiber size of 3″ in diameter. We extracted the one-dimensional spectra from the SDSS archive of the sixth data release (DR6; Adelman-McCarthy et al. 2008). The two spectra agree very well with each other, and both are in an excellent agreement with the SDSS photometric data (see Figure 1). This indicates that (1) the SDSS spectrophotometric calibration is reliable and (2) the quasar did not vary significantly between the SDSS photometric and spectroscopic observations. We stacked the two SDSS spectra, and identified broad emission lines (BELs) in Mg II, C III], and Hγ, and narrow emission lines (NELs) in [O II]λ3727, [Ne III]$\lambda\lambda$3869, 3968, and [Ne V]$\lambda\lambda$3346, 3426 from the quasar. The quasar redshift of $z_Q = 1.047 \pm 0.001$ is measured from the NELs. The SDSS spectrum, together with the infrared through optical to ultraviolet photometric data (Section 2.2) and MMT spectrum (Section 2.3) shown in Figure 1, is very red with a dramatic drop

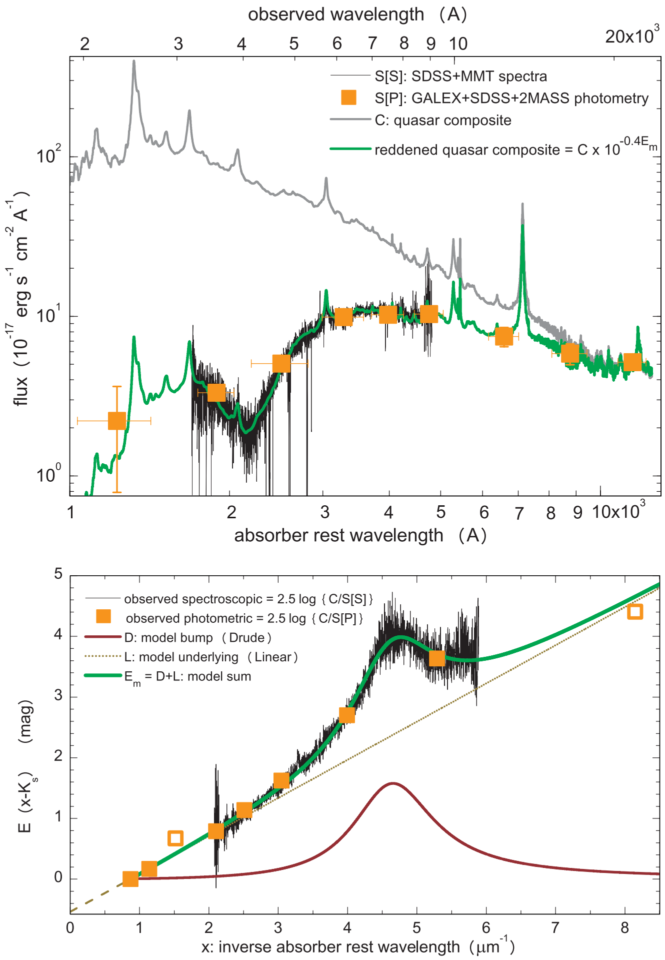

Figure 1. Upper: the observed data of SDSS J1007+2853. The spectrum is the combination of 1 MMT and 2 SDSS spectra. The quasar composite spectra, including the original spectrum and that reddened with the best-fit extinction curve displayed in the lower panel, are overplotted for comparison. Lower: the observed and modeled extinction curve of SDSS J1007+2853G.

(A color version of this figure is available in the online journal.)

shortward of the Mg II BEL, suggesting the presence of heavy dust extinction.

2.2. *Broadband Photometric Data*

We collected broadband photometric data of SDSS J1007+2853 from available large surveys, from radio (FIRST, White et al. 1997; the National Radio Astronomy Observatory Very Large Array Sky Survey or NVSS, Condon et al. 1998) through near-infrared (the Two Micron All Sky Survey or 2MASS, Skrutskie et al. 2006), and the optical (SDSS, York et al. 2000) to ultraviolet (the *Galaxy Evolution Explorer* or *GALEX*, Martin et al. 2005). The results are summarized in Table 1. The radio emission varied by about 45% at 5σ level within 4 months in the quasar rest frame. The radio variability between the NVSS and FIRST should be secure, because the beam size of NVSS (FWHM$_N$ = 45″) is much larger than that of FIRST (FWHM$_F$ = 5″), and the quasar is brighter in the FIRST image. The near-IR and the optical photometric data (Figure 1) join smoothly, suggesting that the quasar did not vary significantly between the 2MASS and SDSS observations. The dramatic flux drop shortward of Mg II BEL appears to slow down somewhere between the SDSS g and u bands, suggesting that an absorption bump occurs there.

Table 1
Photometric Data of SDSS J1007+2853

Band	Flux/Magnitude	Date–Observation	Survey
20 cm	6.80 ± 0.50 mJy	1994-01-11	NVSS
20 cm	9.82 ± 0.16 mJy	1993-04-29	FIRST
NUV	22.656 ± 0.539 mag	2005-02-19	*GALEX*
u	21.175 ± 0.089 mag	2004-05-14	SDSS
g	20.101 ± 0.025 mag	2004-05-14	SDSS
r	18.766 ± 0.020 mag	2004-05-14	SDSS
i	18.304 ± 0.017 mag	2004-05-14	SDSS
z	17.886 ± 0.025 mag	2004-05-14	SDSS
J	16.574 ± 0.140 mag	1998-02-02	2MASS
H	15.735 ± 0.152 mag	1998-02-02	2MASS
K_s	14.812 ± 0.097 mag	1998-02-02	2MASS

2.3. *MMT Spectrum*

A follow-up spectroscopic observation of SDSS J1007+2853 was obtained at 2008 March 30 using the 6.5 m MMT. We used the Blue Channel Spectrograph operated with a 800 g mm^{-1} grating. A slit width of 1$''$.0 is chosen to match the seeing. This setting provides a wavelength coverage of $\lambda \sim 3200$–5200 Å and a spectral resolution of FWHM ≈ 2.3 Å as measured from the comparison lamp lines. One exposure of 1500 s was taken. The CCD reductions, including bias subtraction, flat–field correction, and cosmic ray removal, were accomplished with standard procedures using IRAF.[7] Wavelength calibration was carried out using He/Ne/Ar lamps. A KPNO standard star was observed for flux calibration. The MMT spectrum, after scaled by a factor of 1.4 to compensate for the aperture effect and the uncertainty of absolute flux calibration, agrees very well with the SDSS spectrum in the common wavelength range of 3800–5200 Å. It is also consistent with the SDSS g- and u-band photometric data. The SDSS and MMT spectra are combined to form one spectrum (Figure 1, upper), which will be used to derive the extinction curve.

3. EXTINCTION CURVE

The traditional approach to determine the wavelength dependent extinction, namely an extinction curve, is the "pair method," which is constructed by comparing the fluxes of a reddened object and an (assumed) identical unreddened object (e.g., FM05). This method is not only widely used for the determination of the extinction curves in the MW and other galaxies in the Local Group, but also for the continuum reddening of active galactic nuclei (AGNs). For the former, comparison is made between the reddened stars and unreddened standard stars of the same spectral type. For the latter, either individual blue AGNs spectrum (e.g., Crenshaw et al. 2001) or their composite spectrum (e.g., Wang et al. 2004; Srianand et al. 2008; Noterdaeme et al. 2009) is used.

We derived the "observed extinction curve" $E_o(x - K_s)$ by a direct comparison of the photometric and spectroscopic data $S(x)$ of SDSS J1007+2853 with the composite quasar spectrum $C(x)$, which is obtained by combining the SDSS composite ($\lambda \leqslant 3000$ Å; Vanden Berk et al. 2001) and the near-infrared template ($\lambda > 3000$ Å; Glikman et al. 2006). We normalized $C(x)$ to $S(K_s)$, the observed flux at the 2MASS K_s band. It is then redshifted to $z_Q = 1.047$ and convolved with the 2MASS, SDSS, and *GALEX* filter transmission profiles to obtain the fluxes at the corresponding bands. We calculated the observed extinction curve as $E_o(x - K_s) = 2.5 \log \frac{C(x)}{S(x)}$. Special attention has been paid to the more serious mismatch problem for determination of extinction curves of quasars than that of stars, which has resulted in misidentification of the 2175 Å bump in quasar spectra in the early years (Pitman et al. 2000). However, this has not been shown as a problem for SDSS J1007+2853. The emission-line spectrum of SDSS J1007+2853 and that of the quasar composite match excellently, as can be judged from comparison between the observed spectrum of the quasar and the reddened composite spectrum, and validated from the smoothness of the observed extinction curve. Note that the bump width of 700 Å is much broader than any BEL. Any mismatch of the emission lines between SDSS J1007+2853 and quasar composite spectrum would give birth to spikes with width similar to BELs, which we do not see in the observed extinction curve.

We used Equation (1) to parameterize the observed extinction curve, $E_m(x - K_s) = \tilde{c_1} + \tilde{c_2}x + \frac{\tilde{c_3}x^2}{(x^2-x_0^2)^2+\gamma^2x^2}$, where $\tilde{c_1} = c_1E(B-V) - E(K_s-V)$, $\tilde{c_2} = c_2E(B-V)$, and $\tilde{c_3} = c_3E(B-V)$. We ignored the *GALEX* NUV data in fitting, since it may be affected by the expected damped Lyα absorption line. We also did not consider the SDSS r-band data in fitting to avoid a possible mismatch of Hα BEL between the observed and template spectra. The data within ± 20 Å of Mg II BEL centroid are also masked for the same reason. We fit jointly the spectroscopic and photometric data with the latter weighted by the band widths. The best-fit model yields

$$\{\tilde{c_1}, \tilde{c_2}, \tilde{c_3}, x_0, \gamma\} = \{-0.55 \pm 0.10, 0.626 \pm 0.06, 3.34 \pm 0.16, 4.656 \pm 0.007, 1.449 \pm 0.031\}$$

in the NAL rest frame. $E_m(x-K_s)$ is overplotted with $E_o(x-K_s)$ in the lower panel of Figure 1 for comparison. The composite spectrum is reddened using $E_m(x - K_s)$, and compared with the observed data in the upper panel of Figure 1.

The extinction curves obtained above are actually "reddening curves." Since extinction rapidly decreases with increasing wavelength into the infrared, we can derive the true extinction curve by extrapolating the reddening curve into $\lambda \to \infty$, $A(x) = E(x - K_s) - \lim_{x\to 0} E(x - K_s) = E(x - K_s) + (0.55 \pm 0.10)$. We also obtain the color excess $E(B - V) = E(B - K_s) - E(V - K_s) = 0.28 \pm 0.03$, and the total-to-selective extinction ratio $R_V \equiv A(V)/E(B - V) = 3.87 \pm 0.08$.

4. ABSORPTION LINES AND IONIC COLUMN DENSITIES

Numerous NALs are detected in the SDSS and MMT spectra of SDSS J1007+2853, allowing us to derive gas-phase column densities of many ions. All of the detected NALs are listed in Table 2, and the NALs of interest are shown in Figure 2. The NALs are unresolved at the resolution of both of the SDSS and MMT spectrographs. We used the rest-frame integrated equivalent widths W and a curve of growth (COG) to estimate column densities. We normalized both of the SDSS and MMT spectra using the best-fit model $C(\lambda) \times 10^{-0.4E_m(\lambda-K_s)}$, and measured NALs from the normalized spectra. A Gaussian profile is used to fit the NALs. The widths of all singly ionized weak NALs are set to be identical, as well as the widths of Al III doublet NALs, which are typically broader than low-ionization lines for damped Lyα absorption line systems (DLAs; e.g.,

[7] IRAF is distributed by the National Optical Astronomy Observatory, which is operated by the Association of Universities for Research in Astronomy, Inc., under cooperative agreement with the National Science Foundation.

Table 2
Ionic Column Densities of SDSS J1007+2853

Ion	Transition	f[a]	W (Å)	log N (cm^{-2})
(1) Isolated weak NALs				
Si II	1808.01	0.0021	0.85 ± 0.21	16.39 ± 0.20
Al III	1854.72	0.5590	1.25 ± 0.24	14.32 ± 0.27
Al III	1862.79	0.2780	$\leqslant 0.66$[e]	$\leqslant 14.00$[e]
Cr II	2056.27	0.1030	0.47 ± 0.10	14.18 ± 0.11
Cr II	2066.16	0.0512	0.26 ± 0.11	14.18 ± 0.20
Fe II	2249.89	0.0018	0.66 ± 0.13	16.04 ± 0.11[b]
Fe II	2260.78	0.0024	0.62 ± 0.10	15.86 ± 0.09[b]
Mn II	2576.88	0.3610	0.94 ± 0.10	13.81 ± 0.07
Mn II	2594.49	0.2800	0.78 ± 0.09	13.80 ± 0.07
Mn II	2606.46	0.1980	0.78 ± 0.09	13.95 ± 0.07
Ti II	3230.12	0.0687	$\leqslant 0.21$[e]	$\leqslant 13.53$[e]
Ti II	3242.92	0.2320	0.27 ± 0.06	13.13 ± 0.10
Ca II	3934.78	0.6270	1.26 ± 0.09	13.31 ± 0.04
Ca II	3969.59	0.3120	0.79 ± 0.06	13.34 ± 0.04
(2) Strong NALs				
Fe II	2344.21	0.1140	2.24 ± 0.19	15.65 ± 0.26[b]
Fe II	2374.46	0.0313	1.92 ± 0.15	15.78 ± 0.16[b]
Fe II	2382.77	0.3200	2.89 ± 0.23	16.15 ± 0.40[b]
Fe II	2586.65	0.0691	2.69 ± 0.12	16.11 ± 0.16[b]
Fe II	2600.17	0.2390	2.85 ± 0.15	15.78 ± 0.21[b]
Mg II	2796.35	0.6160	3.47 ± 0.18	15.91 ± 0.27
Mg II	2803.53	0.3060	3.41 ± 0.17	16.11 ± 0.25
Mg I	2852.96	1.8300	2.25 ± 0.16	13.88 ± 0.14
(3) Blended weak NALs				
Zn II	2026.14	0.5010	0.45 ± 0.15[c]	13.49 ± 0.17[c]
Zn II	2062.66	0.2460	$\leqslant 0.30$[d,e]	$\leqslant 13.51$[e]

Notes.
[a] Oscillator strength adopted from York et al. (2006).
[b] The best-fit Fe^+ column density is log $N_{\rm Fe\,II} = 15.95$ cm^{-2} and the internal velocity dispersion $b \approx 75$ km s^{-1} (see Section 4 and Figure 3).
[c] W(Zn II λ2026) and N(Zn II λ2026) are likely overestimated, as discussed in Section 4.
[d] Error in W(Zn II λ2062) is estimated as the error of W(Cr II λ2056) (York et al. 2006).
[e] Quoted as the 3σ upper limit.

Wolfe et al. 2005). The NALs within the common wavelength range of the MMT and SDSS spectra are measured in the MMT spectrum, since both of the resolution and the signal-to-noise ratio (S/N) of the MMT spectrum are higher than that of the SDSS spectrum. The velocity profiles of interested NALs are displayed in Figure 2, and the derived equivalent widths are given in Table 2.

Jenkins (1986) has shown that the standard, single-component Gaussian COG can be used to analyze interstellar NALs, if many lines with similar characteristics are incorporated. Very nearly correct values of total column density N can be derived even when different lines have large variations in the central optical depth, τ_0, and the interval velocity dispersion, b. We detected seven Fe II NALs in the normalized spectrum of SDSS J1007+2853: two weak lines Fe II $\lambda\lambda$2249, 2260 and five strong lines Fe II $\lambda\lambda$2344, 2374, 2382, 2586, 2600. All of the seven Fe II NALs arise from absorption of Fe^+ at the ground level, and thus have the same column density, $N_{\rm Fe\,II}$, and the same internal velocity dispersion, b. The fact, W(Fe II $\lambda\lambda$2249, 2260) $\approx \frac{1}{3}$W(Fe II $\lambda\lambda$2344, 2374, 2382, 2586, 2600), indicates that the two weak Fe II NALs are not severely deviated from the linear part of the COG, while the five strong Fe II NALs are heavily saturated. The combination of the seven Fe II NALs are used to derive the COG. We calculated theoretical COG of various b values and searched for the best match between the calculated COG and the measured W of the seven Fe II NALs, with both of b and $N_{\rm Fe\,II}$ as free parameters. This was done by generating a large number of two-dimensional grids with different b and $N_{\rm Fe\,II}$ values, with steps of 1 km s^{-1} in b and 0.01 dex of cm^{-2} in $N_{\rm Fe\,II}$, and finding the best fit by minimizing the reduced χ^2. Both parameters can be well constrained with $b \approx 75$ km s^{-1} and log $N_{\rm Fe\,II} \approx 19.95$ cm^{-2} and 1σ errors less than 5 km s^{-1} and 0.05 cm^{-2}, respectively, as shown in Figure 3.

We derived the column densities of other ions using the best-fit COG and the measured NAL equivalent widths. The detected NALs can be split into three categories (see Table 2):

Isolated Weak NALs are either slightly saturated or located on the linear part of COG. Derivation of the column densities of these ions is straightforward and is, in general, more reliable compared to the other two categories listed below. Reliability of the derived column densities is verified by the good agreement of N measured from different lines in multiplets—all but Si II λ1808 are in the multiplets, and N values of all ions but Al III derived from the multiplets agree within errors. The disagreement between $N_{\rm Al\,III\,\lambda1854}$ and $N_{\rm Al\,III\,\lambda1862}$ is understandable, since the internal velocity dispersion b of high-ionization lines is often larger than that of low-ionization lines (e.g., Wolfe et al. 2005).

Strong NALs are severely saturated, according to the derived COG shown in Figure 3. The internal velocity b of neutral Mg is much less than that of singly ionized ions in the ISM of the MW (e.g., Spitzer 1978). Upon that, $N_{\rm Mg\,I\,\lambda2852}$ given in Table 2should be taken as a lower limit to $N_{\rm Mg^0}$.

Blended Weak NALs include the λ2026 blend of Zn II and Mg I, and the λ2062 blend of Zn II and Cr II. We removed the contribution of Cr II from the λ2062 blend by averaging W(Cr II λ2056) and W(Cr II λ2066), because the oscillator strength of Cr II λ2062 is about the average of that of Cr II λ2056 and Cr II λ2066 (e.g., Khare et al. 2004), and the latter two lines are nearly located on the linear part of the COG (Figure 3). W(Mg I λ2026) is estimated from the $N_{\rm Mg\,I\,\lambda2852}$ and removed from the λ2026 blend. $W(Zn\ \lambda2026)$ and then $N_{Zn\lambda2026}$ estimated this way should be treated more properly as an upper limit to N_{Zn^+}because W(Mg I λ2026) is very likely underestimated.

We estimated the error of N incorporating both of the fitting error of b and the measurement uncertainties of W. N is very sensitive to W for weak NALs, which are located on or near the linear part of the COG. The main contribution to the error of N for weak NALs is the measurement error of W due to the low S/N of the SDSS and MMT spectra. The errors of column densities estimated only from strong NALs, including Mg II and Mg I, are relatively large, since N is not sensitive to W for NALs located on the flat part of the COG.

5. DISCUSSION

5.1. Location of the 2175 Å Absorber

The dusty material we see in SDSS J1007+2853 can be located anywhere along the line of sight toward the quasar, including the ISM of an intervening galaxy, the ISM of the host galaxy of the quasar, or the dusty torus near the quasar nucleus postulated by the AGN unification scheme (e.g., Urry & Padovani 1995). Detection of the 2175 Å bump and the NAL system allows us to nail down its location. The bump peaks at $\lambda_p = 2148 \pm 10$ Å in the NAL rest frame, within the range detected in the MW (see Figure 4(b)). Both of the NALs and the extinction should arise from the same material

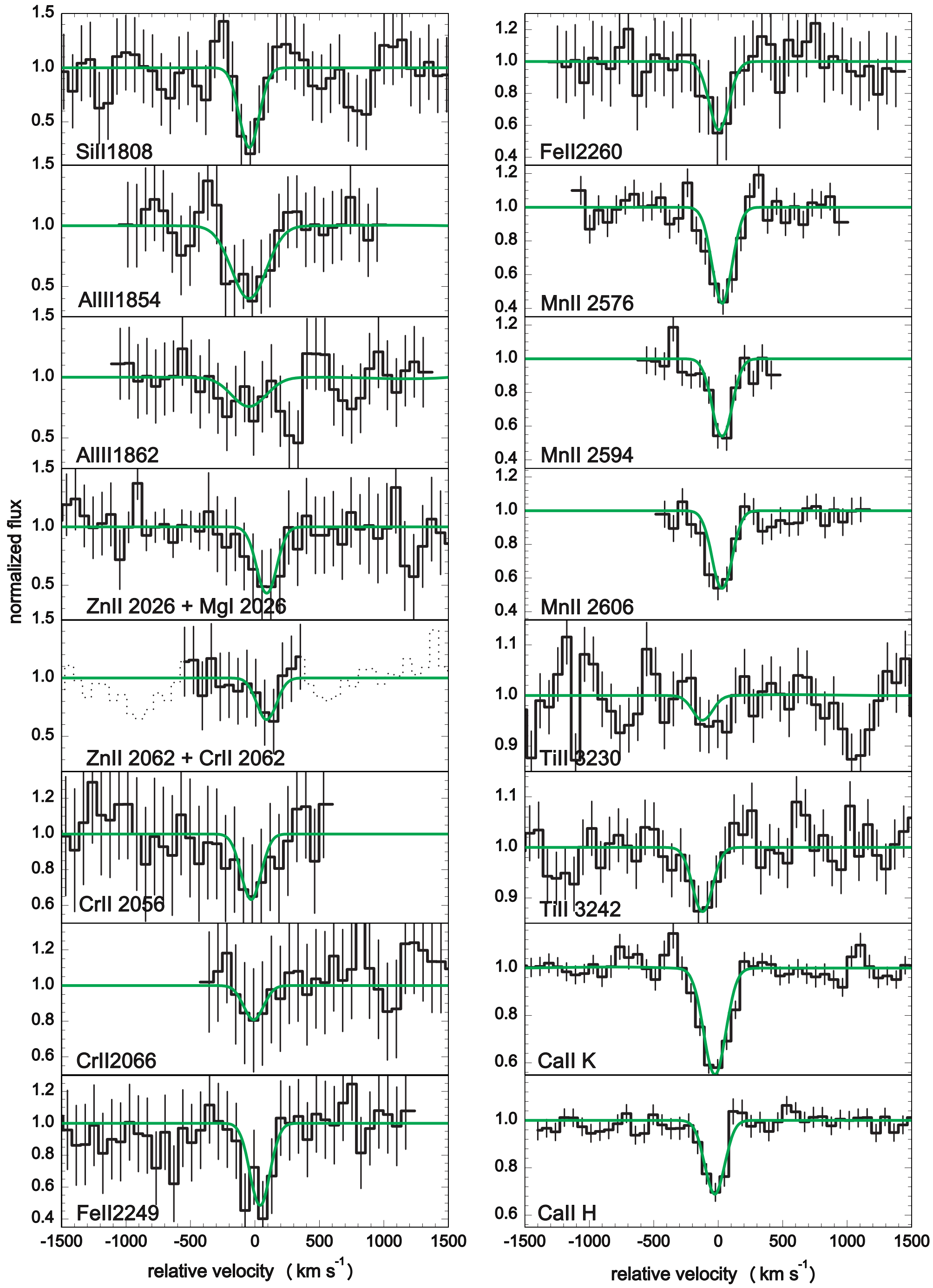

Figure 2. Velocity plot of the absorption-line spectrum of SDSS J1007+2853G. Only weak lines are shown. The velocity origin corresponds to $z_G = 0.8839$. (A color version of this figure is available in the online journal.)

with a velocity of $v \approx 2.5 \times 10^5$ km s^{-1} with respect to the quasar systematic redshift. Such a velocity is too large either for the ISM of the host galaxy or for the presumed torus of the quasar. The dusty torus possibility is also unfavored by the radio observations. The large amplitude radio variability imply a very high brightness temperature of $T_B \gtrsim 3.5 \times 10^{13}$ K, much higher than the inverse Compton limit of $T_C = 10^{13}$ K. The radio jets in SDSS J1007+2853 should be relativistic and beaming toward the observer with an inclining angle of $i \lesssim 17^\circ.5$ (e.g., Zhou et al. 2006), i.e., the quasar is observed nearly face-on. This is contrary to the prediction of the AGN unification models. Therefore, the dusty absorber must be an intervening galaxy.

5.2. Dust Properties and Carrier of the 2175 Å Absorption Bump

The advantage to the extinction curve parameterization in Section 3 allows for meaningful comparisons between SDSS J1007+2853G and the MW. Such comparisons are shown in Figure 4 with the FM07 sample of 328 Galactic interstellar curves, which virtually includes all of the Galactic stars with high quality broadband data. Evidently, the strength of the 2175 Å bump of SDSS J1007+2853G is stronger than all of the known MW sight lines. It is about 2.5 times of the MW average. Yet the peak position and width of the bump of SDSS

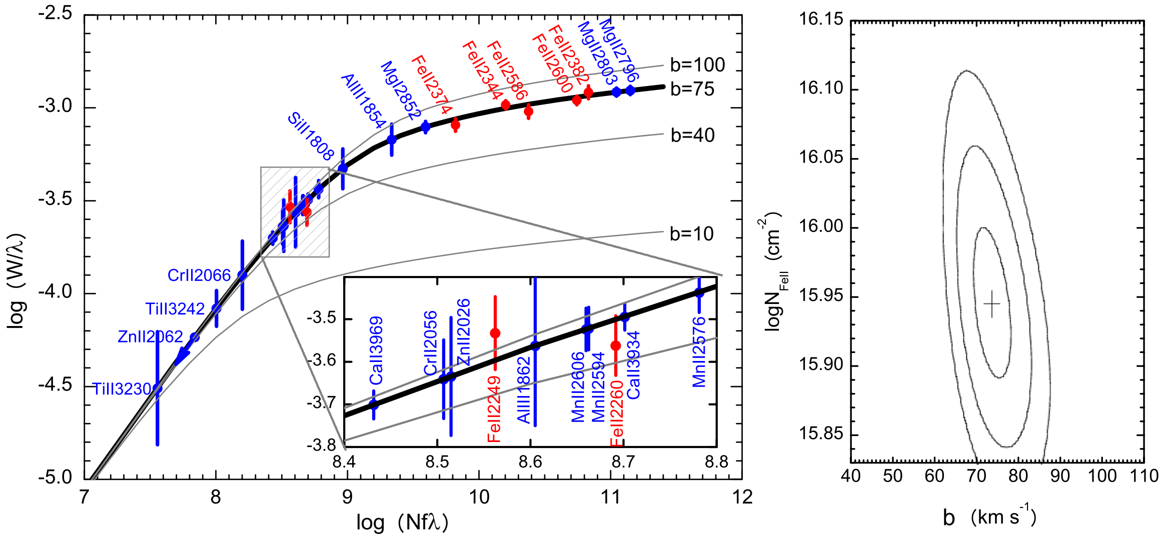

Figure 3. Best-fit COG using the seven Fe II NALs is shown in the thick black line in the left panel, and 1, 2, and 3σ confidence levels are shown in the right panel. Column densities of other ions are estimated using the best-fit COG. See Section 4 for detailed description.

(A color version of this figure is available in the online journal.)

J1007+2853G are within the ranges that are detected in MW. Its total-to-selective extinction $R_V \approx 3.87$ is a little larger than that found in the MW, whose average value is $R_V = 3.24$ with a standard deviation of 0.63 (FM07).[8] This suggests that SDSS J1007+2853G is more abundant in large size dust grains than the MW. Interestingly, SDSS J1007+2853G is located almost exactly on the c_1–c_2 correlation relation found in the MW (FM07), though both of the intercept c_1 and the slope c_2 of the linear underlying extinction are much larger than that of the MW. It is important, however, to point out that the estimation of R_V depends strongly on the assumed intrinsic continuum slope of the background quasar.

Whereas the modeled parameters of the 2175 Å bump are not sensitive to the assumed continuum shape of the background quasar, and thus are much more reliable than that of the underlying extinction. The unprecedentedly strong bump strength can give a strict constraint to the 2175 Å carrier. Using Equation (2), we obtained a conservative estimate of the absorber column density of $N_{2175} \gtrsim 3.5 \times 10^{16}$ cm^{-2}, where we adopted an upper limit of $f_{2175} \lesssim 1$ to the oscillator strength per absorber (see Section 1; cf. Draine 1989) and did not take into account of the starlight contribution from both of the intervening and the host galaxy. The relative abundance of the bump absorber in SDSS J1007+2853G with respect to Zn is $\frac{N_{2175}}{N_{\rm Zn\,II\,\lambda2062}} > 1082$, significantly larger than the relative solar values of $\left\{\frac{N_{\rm Mg}}{N_{\rm Zn}}, \frac{N_{\rm Si}}{N_{\rm Zn}}, \frac{N_{\rm Fe}}{N_{\rm Zn}}\right\}_\odot \approx \{810, 750, 680\}$. Therefore, we can exclude Mg, Si, and Fe as the main carrier of the 2175 Å bump, provided that Zn is not heavily depleted onto dust grains in SDSS J1007+2853G. Consequently, the only candidate element left is carbon. It has been suggested that the best candidate carrier of the 2175 Å bump is some form of graphitic carbon, most likely polycyclic aromatic hydrocarbons (PAHs; see Draine 2003 for a review). Our discovery strongly favors the PAH model. The age at redshift $z = 0.8839$ of the absorption galaxy was about 6.2 Gyr, less than half of the current cosmic age. This implies that a galaxy more mature than the MW already existed at such an early epoch, which is not only of great importance to cosmic dust evolution, but also of great astrobiological interest (Wang et al. 2004). The above conclusion depends on the assumption that zinc shows little affinity for dust grains as in the MW, where $N_{\rm Zn}$ is often used as a surrogate of N_H to estimate depletions of other elements when total H column density is not available (e.g., Tielens 2005). However, the dust depletion patterns in SDSS J1007+2853G might be quite different from that in the MW, as will be discussed in Section 5.3. Ultraviolet spectroscopy is needed to confirm the conclusion with direct measurement of N_H from the expected damped Lyman absorption lines, which can be achieved by *Hubble Space Telescope* (*HST*).

5.3. Dust Depletion and Nucleosynthesis

Besides Zn, we have obtained gas-phase column density measurements of X = {Mn, Cr, Si, Fe, Mg, Ti, Ca} from NALs (Table 2). We derived the relative abundances of X/Zn with respect to the solar values, $[X/{\rm Zn}] \equiv \log(X/{\rm Zn}) - \log(X/{\rm Zn})_\odot$, and provided comparison in Figure 5 to that observed in the cool and warm diffused clouds toward ζ Oph (Savage & Sembach 1996; hereafter $[X/{\rm Zn}]_G$ for the values in SDSS J1007+2853G, and $[X/{\rm Zn}]_{c\zeta}$ and $[X/{\rm Zn}]_{w\zeta}$ for the cool and warm ζ clouds, respectively).[9] Refractory elements are much more heavily depleted in the cool diffuse clouds than in the warm diffused clouds (Savage & Sembach 1996). The relative abundance pattern of SDSS J1007+2853G resembles the warm more than the cool clouds, and $[X/{\rm Zn}]_G \lesssim [X/{\rm Zn}]_{w\zeta}$ for all of the measured elements. This suggests that as a whole dust depletion is less in SDSS J1007+2853G than in MW. In fact, the estimated elemental depletion is so low, for instance, silicon is hardly depleted. It is puzzling that only such a small amount of material is left for dust grains. This appears to be inconsistent with the extremely strong 2175 Å bump strength in this system. Detailed inspection of the difference of the relative abundance pattern

[8] The often quoted average value is $R_V = 3.1$ (e.g., Draine 2003), which is slightly less than that given in FM07.

[9] The values of ρ Oph cloud are potentially better as a comparison, where dusty material has been suggested to be contained primarily in large grains resulting in ineffective scatters of the optical and ultraviolet light (Snow & Jenkins 1980). However, only upper limit to zinc column density is available (Snow & Joseph 1985).

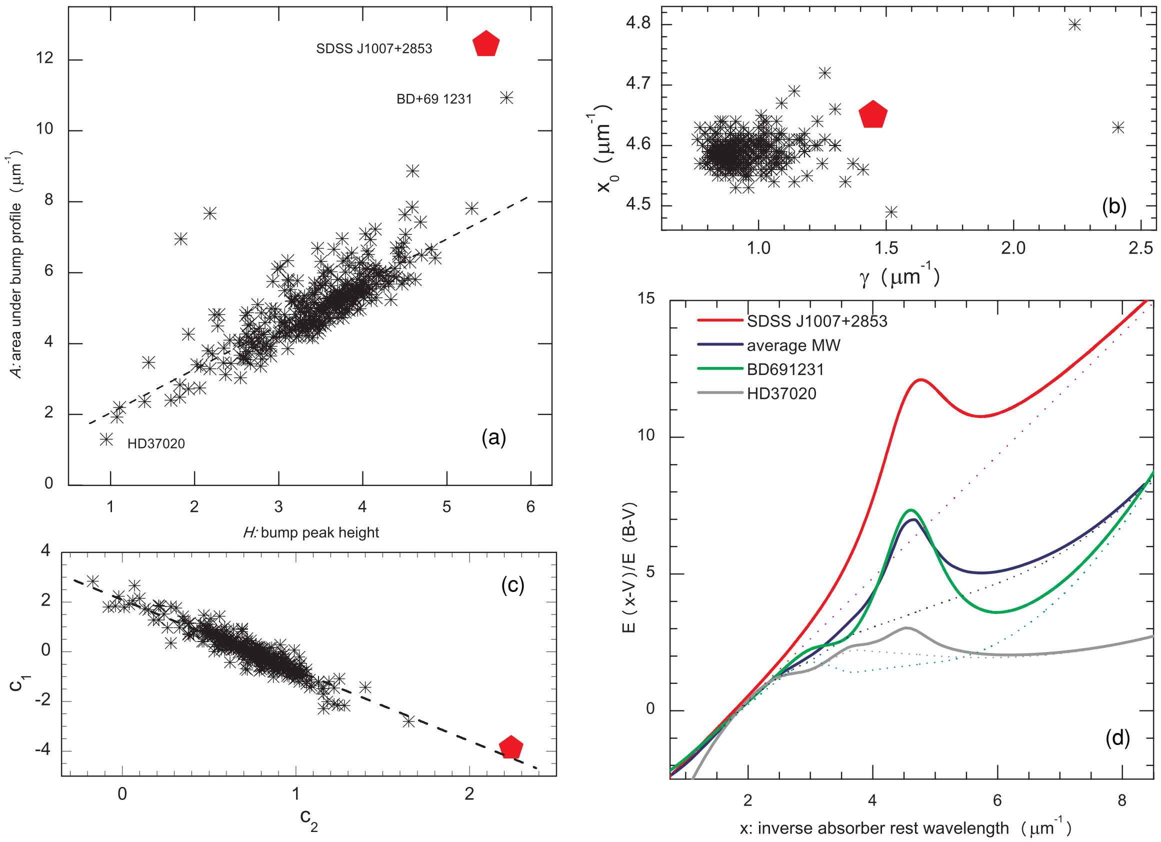

Figure 4. Comparisons of extinction curve parameters of SDSS J1007+2853G with the 328 Galactic stars from FM07. The bump strength of SDSS J1007+2853G is stronger than that in all of the Galactic extinction curves (a), while both of the peak position and width of the bump of SDSS J1007+2853G are within the ranges found in MW (b). (c) SDSS J1007+2853G is located in the c_i–c_2 correlation relation found in MW, though the intercept c_1 and slope c_2 of the underlying linear extinction are both much larger than that in the MW curves. (d) Direct comparison of modeled extinction curves between SDSS J1007+2853G and the Galactic average curve and two individual curves with the strongest (BD+69 1231) and weakest (HD37020) bump.

(A color version of this figure is available in the online journal.)

between SDSS J1007+2853G and MW reveals $\{[X/\mathrm{Zn}]_G - [X/\mathrm{Zn}]_{c\zeta}\} \approx \{\underline{0.22}, \overline{0.47}, \overline{0.64}, \overline{1.2}, \underline{1.2}, \underline{1.3}, \underline{1.7}\}$ for $X = \underline{\mathrm{Mn}}$, $\overline{\mathrm{Mg}}$, $\overline{\mathrm{Si}}$, $\overline{\mathrm{Ca}}$, $\underline{\mathrm{Fe}}$, $\underline{\mathrm{Cr}}$, and $\underline{\mathrm{Ti}}$, where "α-elements" are labeled with upper-lineations and "Fe-peak elements" with lower-lineations. The two classes of elements have different origins: the α-elements are synthesized by the supernovae (SNe) II of massive stars, while the Fe-peak elements are mainly generated by SNe Ia with low-mass progenitors. The observed [X/Zn] of SDSS J1007+2853G can be similar to the MW for different class of elements, and be very different for the same class of elements. This can originate either from different dust depletion pattern, or from different nucleosynthetic processes. Further studies of this system through high-resolution optical and also UV spectroscopy in the future will help us to derive absolute abundances to distinguish between the two classes of elements and understand the nature of dust grains and also 2175 Å carriers in SDSS J1007+2853G.

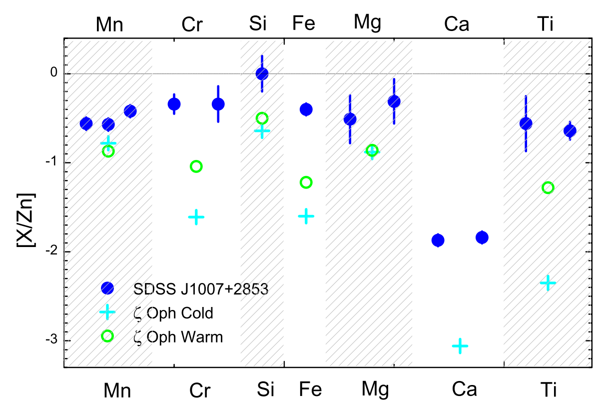

Figure 5. Dust depletion pattern of SDSS J1007+2853G in comparison with that of the ζ Oph diffused clouds.

(A color version of this figure is available in the online journal.)

Many thanks to Stefanie Komossa and Jianmin Wang for helpful discussion. We thank the anonymous referee for constructive comments and suggestions. This work was supported by NSF AST-0451407 and AST-0451408, NASA NNG05G321G and NNG05GR41G, and the University of Florida. H.Z. acknowledges support from the Alexander von Humboldt Foundation, from NSF-10533050, and from program 973 (2007CB815405). This work has made use of the data obtained by SDSS and MMT.

Funding for the SDSS and SDSS-II has been provided by the Alfred P. Sloan Foundation, the Participating Institutions, the National Science Foundation, the US Department of Energy, the National Aeronautics and Space Administration, the Japanese Monbukagakusho, the Max Planck Society, and the Higher Education Funding Council for England. The SDSS Web Site is http://www.sdss.org/.

The SDSS is managed by the Astrophysical Research Consortium for the Participating Institutions. The Participating

Institutions are the American Museum of Natural History, Astrophysical Institute Potsdam, University of Basel, University of Cambridge, Case Western Reserve University, University of Chicago, Drexel University, Fermilab, the Institute for Advanced Study, the Japan Participation Group, Johns Hopkins University, the Joint Institute for Nuclear Astrophysics, the Kavli Institute for Particle Astrophysics and Cosmology, the Korean Scientist Group, the Chinese Academy of Sciences (LAMOST), Los Alamos National Laboratory, the Max-Planck-Institute for Astronomy (MPIA), the Max-Planck-Institute for Astrophysics (MPA), New Mexico State University, Ohio State University, University of Pittsburgh, University of Portsmouth, Princeton University, the United States Naval Observatory, and the University of Washington.

The 6.5 m MMT telescope is operated by the MMT observatory, a joint venture of the smithsonian institution and the University of Arizona.

REFERENCES

Adelman-McCarthy, J. K., et al. 2008, ApJS, 175, 297
Cartledge, S. I. B., et al. 2005, ApJ, 630, 355
Condon, J. J., Cotton, W. D., Greisen, E. W., Yin, Q. F., Perley, R. A., Taylor, G. B., & Broderick, J. J. 1998, AJ, 115, 1693
Crenshaw, D. M., Kraemer, S. B., Bruhweiler, F. C., & Ruiz, J. R. 2001, ApJ, 555, 633
Diplas, A., & Savage, B. D. 1994, ApJS, 93, 211
Draine, B. 1989, in IAU Symp. 135, Interstellar Dust, ed. L. J. Allamandola & A. G. G. M. Tielens (Dordrecht: Kluwer), 313
Draine, B. T. 2003, ARA&A, 41, 241
Ellison, S. L., et al. 2006, MNRAS, 372, L38
Fitzpatrick, E. L., & Massa, D. 1986, ApJ, 307, 286 (FM86)
Fitzpatrick, E. L., & Massa, D. 1990, ApJS, 72, 163 (FM90)
Fitzpatrick, E. L., & Massa, D. 2005, AJ, 130, 1127 (FM05)
Fitzpatrick, E. L., & Massa, D. 2007, ApJ, 663, 320 (FM07)
Glikman, E., Helfand, D. J., & White, R. L. 2006, ApJ, 640, 579
Jenkins, E. B. 1986, ApJ, 304, 739
Khare, P., Kulkarni, V. P., Lauroesch, J. T., York, D. G., Crotts, A. P. S., & Nakamura, O. 2004, ApJ, 616, 86
Krühler, T., et al. 2008, ApJ, 685, 376
Lequeux, J., Maurice, E., Prevot-Burnichon, M.-L., Prevot, L., & Rocca-Volmerange, B. 1982, A&A, 113, L15
Martin, D. C., et al. 2005, ApJ, 619, L1
Noterdaeme, P., Ledoux, C., Srianand, R., Petitjean, P., & Lopez, S. 2009, A&A, 503, 765
Pitman, K. M., Clayton, G. C., & Gordon, K. D. 2000, PASP, 112, 537
Savage, B. D., & Sembach, K. R. 1996, ARA&A, 34, 279
Schady, P., et al. 2007, MNRAS, 377, 273
Schlegel, D. J., Finkbeiner, D. P., & Davis, M. 1998, ApJ, 500, 525
Skrutskie, M. F., et al. 2006, AJ, 131, 1163
Snow, T. P., & Joseph, C. L. 1985, ApJ, 288, 277
Snow, T. P., Jr., & Jenkins, E. B. 1980, ApJ, 241, 161
Spitzer, L. 1978, Physical Processes in the Interstellar Medium (New York: Wiley Interscience), 333
Srianand, R., Gupta, N., Petitjean, P., Noterdaeme, P., & Saikia, D. J. 2008, MNRAS, 391, L69
Stecher, T. P. 1965, ApJ, 142, 1683
Tielens, A. G. G. M. 2005, The Physics and Chemistry of the Interstellar Medium, ed. A. G. G. M. Tielens (Cambridge: Cambridge Univ. Press)
Urry, C. M., & Padovani, P. 1995, PASP, 107, 803
Vanden Berk, D. E., et al. 2001, AJ, 122, 549
Wang, J., Hall, P. B., Ge, J., Li, A., & Schneider, D. P. 2004, ApJ, 609, 589
White, R. L., Becker, R. H., Helfand, D. J., & Gregg, M. D. 1997, ApJ, 475, 479
Whittet, D. C. B. 1992, Science, 257, 1148
Wolfe, A. M., Gawiser, E., & Prochaska, J. X. 2005, ARA&A, 43, 861
York, D. G., et al. 2000, AJ, 120, 1579
York, D. G., et al. 2006, MNRAS, 367, 945
Zhou, H., Wang, T., Wang, H., Wang, J., Yuan, W., & Lu, Y. 2006, ApJ, 639, 716